ACI STRUCTURAL JOURNAL TECHNICAL PAPER

Title No. 122-S24

Autoregularized Model of Compressive Behavior of Structural Wall Boundary Elements

by Carlos A. Arteta, Jefferson Piedrahita, and Christopher L. Segura Jr.

The adequate seismic behavior of slender reinforced concrete (RC) structural walls relies heavily on the effectiveness of the boundary element (BE) in providing stable resistance against combined axial and flexural-shear compression demands resulting from gravity loading and lateral earthquake deformations. The geometric properties of the BE, including thickness and confined length, as well as the arrangement, detailing, and quantity of transverse reinforcement, play crucial roles in achieving a stable compressive response. Laboratory tests on isolated BE specimens subjected to uniform axial compression or cyclic axial tension and compression have been instrumental in understanding the influence of these variables on the compressive behavior of wall BEs. This study uses a database of experimental results from 45 rectangular BE specimens to establish empirical relationships between compressive force and strain, accounting for geometric and transverse reinforcement design parameters. A novel auto-regularizing model is proposed to estimate the compressive behavior within the damaged zone of a BE, based on its geometry and transverse reinforcement.

Keywords: boundary element (BE); compression test; fracture energy in compression; regularization; reinforced concrete (RC); strain capacity model; structural wall.

INTRODUCTION

The seismic performance of reinforced concrete (RC) structural walls under combined axial and flexural-shear demands resulting from gravity and earthquake loading depends on the wall geometry and detailing of the critical section. For example, where flexural-compression yielding is expected, proper consideration of the boundary element (BE) thickness and the arrangement and quantity of transverse reinforcement is critical to ensure a stable response in the compressed region of the wall.

Damage to BEs of RC shear walls observed after the 2010 Chile and 2011 New Zealand earthquakes was characterized by loss of concrete cross section, fracture and/or opening of transverse reinforcing ties, and longitudinal bar buckling (Wallace et al. 2012; Sritharan et al. 2014). Further, after the Chile earthquake, Wallace et al. (2012) reported that the damaged zone was of limited height (between one to three times the wall thickness), suggesting a relatively brittle failure mechanism. Recent experimental testing confirmed that thin RC walls may exhibit flexural-compression failure at modest drift demands due to significant plastic deformations in the compression edge of the wall (Segura and Wallace 2018a). These observations exposed deficiencies in the detailing outlined by then-current building codes, leading to changes aimed at addressing the shortcomings in seismic design provisions for slender RC walls (ACI Committee 318 2014; Welt et al. 2017; Segura and Wallace 2018a; Arteta and Moehle 2023).

The compressive deformation capacity of the BE of a wall, which may ultimately limit the lateral drift capacity of the, is influenced by its geometry and the quantity and arrangement of steel reinforcing bars. Researchers and practitioners typically estimate the compressive capacity of BEs using confinement models derived from laboratory tests on square and circular specimens subjected to uniform axial compression (Sheikh and Uzumeri 1982; Razvi and Saatcioglu 1999). A smaller number of tests have been conducted on specimens with rectangular cross sections that may be more representative of the BE in a slender wall (Mander et al. 1988b; Saatcioglu and Razvi 1992). However, as pointed out by Arteta and Moehle (2023), a shortcoming of these models is that they were developed without considering the applicable gauge length over which compressive strains are reported, despite predicting stress-strain behaviors that include strain softening. Furthermore, laboratory tests used to derive confinement models to estimate the compressive capacity of a structural wall BE do not properly consider all the transverse reinforcement details allowed by RC design standards (for example, ACI 318), such as longitudinal reinforcing bars that are not restrained by a hoop leg or a crosstie.

The present study curates and analyzes a database of experimental results from 45 rectangular specimen tests conducted by various researchers in the 1980s and the 2010s. In addition to the full compression force-shortening relationship, other variables of interest are the transverse reinforcement layout, the volumetric transverse reinforcement ratio, the height over which damage is observed, and the fracture energy.

The model presented herein enables the calculation of the compressive force-strain relationship for rectangular RC prisms representative of BEs of structural walls considering three types of transverse reinforcement layouts: one in which some longitudinal bars are not restrained laterally by a crosstie or hoop leg, and two other layouts in which a crosstie or hoop laterally supports all longitudinal bars. The model predicts the uniaxial monotonic compressive behavior over a wide range of BE detailing, including ACI 318-compliant ordinary boundary element (OBE) and special boundary

ACI Structural Journal, V. 122, No. 2, March 2025.
MS No. S-2023-281.R1, doi: 10.14359/51743302, received August 3, 2024, and reviewed under Institute publication policies.

element (SBE) detailing, as well as non-ACI 318-compliant detailing. A novel aspect of the model is that the post-peak strain response adjusts according to the plastic length input by the user, a process termed "autoregularization" herein, referring to mesh-independent finite element modeling methods (Coleman and Spacone 2001). The model can potentially improve the estimation of the deformation capacity of slender walls vulnerable to flexural-compressive failure.

RESEARCH SIGNIFICANCE

In contemporary seismic design, slender shear walls are primarily designed to exhibit flexural response, with compression failure being the predominant mode of failure in practice (Lowes et al. 2012; Birely et al. 2015). A semi-empirical model is presented that provides a means to better quantify the compressive capacity of the boundary element in slender walls, including the post-peak response and damage localization. The model accounts for the wall geometry (for example, compression zone thickness) and the arrangement and quantity of steel reinforcement. A unique feature of the model is that it allows the user to select the desired length over which to model the compressive response, adjusting the post-peak relationship accordingly.

BACKGROUND AND PREVIOUS RESEARCH

Confinement models commonly used to predict the compressive behavior of RC sections have been derived mostly from laboratory tests on square and circular specimens. However, BEs in slender walls are typically rectangular-shaped, and their compressive deformation capacity may be substantially smaller than predicted by common confinement models due to the inferior confining capabilities of rectangular sections (Arteta and Moehle 2023). Experimental testing of rectangular RC prisms in compression began in the mid-1980s with Mander et al. (1988a). They conducted monotonic compression tests on rectangular RC prisms representative of the flange of hollow columns and proposed a model to simulate the expected stress-strain behavior of the confined concrete (Mander et al. 1988b). All reported test specimens had cross sections reinforced by perimeter hoops with crossties or internal hoops providing lateral support for every longitudinal bar.

Between 2010 and 2020, there was a significant increase in the number of tests on rectangular prisms, representative of boundary elements at the edge of slender walls; the effort, motivated by field observations of flexural-compression failures after the 2010 Chile and 2011 New Zealand earthquakes, aimed at testing their axial force-displacement performance. For example, after the Chile earthquake, Creagh et al. (2010) and Acevedo et al. (2010) tested scaled models representative of thin BEs. Between 2012 and 2014, Arteta et al. (2014) and Arteta (2015) conducted monotonic compression testing on full-scale rectangular prisms compliant with BE requisites for special structural walls per ACI 318-11 (ACI Committee 318 2011). Massone et al. (2014), Taleb et al. (2016), Welt et al. (2017), and Tripathi et al. (2020) carried out experimental campaigns that included pure monotonic compression tests, accompanied by compression tests with pre-tension or with cyclic loading protocols.

A consistent result from these tests campaigns is that strain softening is observed in the compressive force-deformation response of rectangular prisms. In a typical monotonic compression test, initial failure is triggered by spalling of the cover concrete, leading to some initial loss of axial force resistance. Where insufficient transverse reinforcement is provided and/or the thickness of the section is inadequate, axial failure may be abrupt after spalling, with little compressive deformation capacity. Conversely, when transverse reinforcement and section geometry are adequate, the confined core may regain strength to offset the loss of axial capacity from cover spalling, and it may sustain force through larger axial compressive deformations. Failure of BE specimens can include opening and/or rupturing hoops and crosstie hooks, buckling of the longitudinal reinforcement, loss of core concrete, and/or out-of-plane instability.

Strain softening results in damage localization and, consequently, non-uniform distribution of strains along the specimen length (Markeset and Hillerborg 1995). Therefore, the reported strains must have an associated gauge length over which they are measured; alternatively, a report of the absorbed energy, referred to herein as the fracture energy in compression, is appropriate. One approach to controlling damage propagation in previous tests has been to reinforce the extreme regions of a test specimen, thus forcing failure to occur within a central test zone of limited height, and then to measure deformations and derive strains as an average along this region. This method is not, however, applied uniformly from one test program to another. For test specimens in the 1980s, the gauge length ranged between 1 and 2.7 times the smallest cross-section dimension. In contrast, post-2010 tests on rectangular prisms, which are generally more representative of the BE of a wall, report the average strain measured over the height of the specimen, resulting in a gauge length range between 4.0 and 8.8 times the smallest cross-section dimension. Further, in early confined prism tests reported in the literature, stability was maintained by: a) using a relatively small height-to-thickness, or aspect ratio (typically around 3.0); and b) restricting the failure zone to the middle third of the specimen height through internal or external strengthening of the end regions. In contrast, the post-2010 specimens with an aspect ratio ranging between 4.0 and 8.0 lack this lateral restraint, with the authors reporting out-of-plane instability after the peak load is attained.

RECTANGULAR PRISMS DATABASE

The RC boundary element database (BEDB) includes specimens tested by Mander et al. (1988a), Massone et al. (2014), Arteta (2015), Taleb et al. (2016), Welt et al. (2017), and Tripathi et al. (2020). These experimental programs included the application of uniform, monotonic compression loading to failure; some tests also included cyclic tension-compression loading or an initial pre-tension load applied to the specimen before compression loading to failure. The BEDB used herein only considers those specimens tested under pure monotonic compression.

Variables of interest

The BEDB is parameterized to evaluate the variables that impact the compressive capacity of the BE of a slender wall to develop a capacity model. Such variables include the BE geometry and the spacing and quantity of transverse reinforcement. Evaluation of the parameterized database leads to three primary variables of interest: (i) *Detail*, a categorical variable that groups data according to the transverse reinforcement layout of the cross section, separating cross sections with untied longitudinal bars from the others; (ii) the experimental damaged zone height (H_{DZ}), over which the strain localization process occurs (Jansen and Shah 1997); and (iii) the volumetric transverse reinforcement ratio in through-the-thickness direction (ρ_x), which correlates with the absorbed energy within the damaged region of the specimens.

Figure 1 provides a graphical representation of these variables. Figure 1(a) depicts three *Detail* groups: 1) cross sections with an outer hoop and internal crossties or additional hoops with unsupported longitudinal bars; 2) cross sections with an outer hoop and all internal longitudinal bars supported laterally by crossties; and 3) cross sections with all bars tied by overlapping hoops (that is, without internal crossties). Other cross-section variables are the gross area (A_g), which is bounded by the specimen length (l_{be}) and thickness (b); the core area, to the outside of the perimeter hoops (A_{ch}), which is defined herein as the product of the core length (b_{cx}) and width (b_{cy}); and A_{shx}, the total area of reinforcing steel in one layer of transverse reinforcement parallel to the through-thickness direction. Figures 1(b) and (c) illustrate the elevation-specific variables, including the total and unsupported height (h and h_u, respectively), the H_{DZ}, and the vertical spacing of transverse reinforcement (s). In general, $h = h_u$, except for the Mander et al. (1988a) specimens, which were restrained laterally to avoid out-of-plane instability. Other variables are described in Table 1.

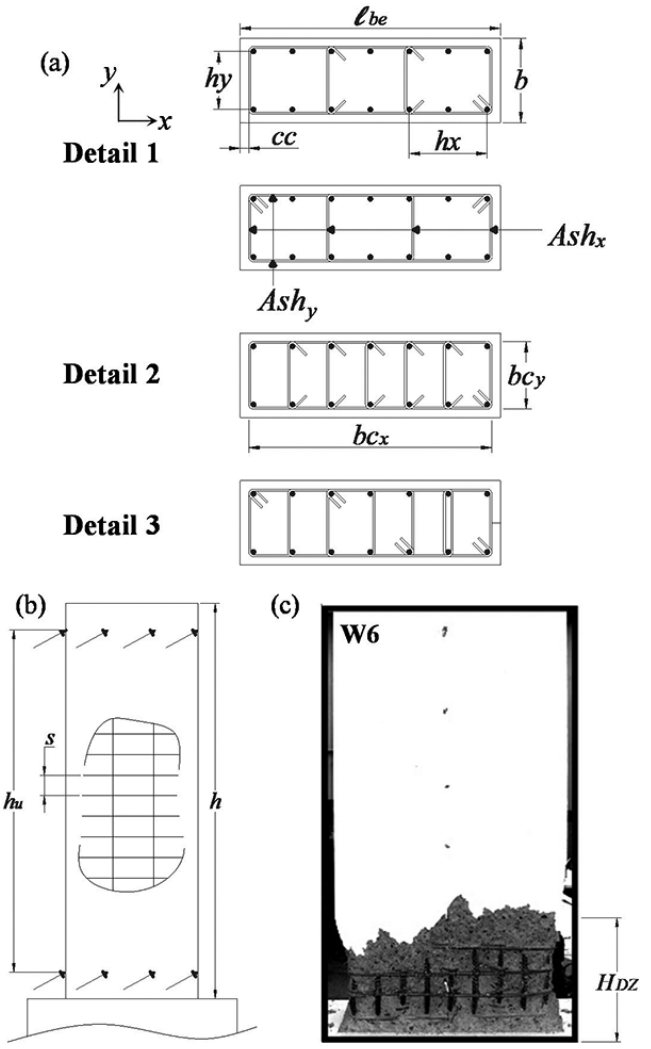

Fig. 1—Representation of relevant variables of BEDB: (a) cross-section variables and organization by Detail*; (b) elevation variables; and (c) damaged zone length.*

RC BEDB

The BEDB comprises 45 experimental tests of rectangular prism specimens representative of structural wall boundary elements. Table 1 summarizes the geometric and reinforcement details of the specimens, organized by author(s), along with summary statistics for each parameter. Measured test-day material properties are f_c', unconfined concrete compressive strength, and f_{yl} and f_{yt}, yield strength of the longitudinal and transverse reinforcement, respectively.

For special BE, ACI 318-19 requires compliance with Eq. (1) and (2)

$$\rho_i = \frac{A_{shi}}{s\,b_{ci}} \geq 0.3\frac{f_c'}{f_{yt}}\left(\frac{A_g}{A_{ch}} - 1\right) \quad (1)$$

$$\rho_i \geq 0.09\frac{f_c'}{f_{yt}} \quad (2)$$

where subscript i identifies either analysis direction; for example, $\rho_x = A_{shx}/sb_{cx}$ represents the through-thickness direction of the cross section; analogously, ρ_y is for the orthogonal direction. Note that Eq. (2) is a lower limit to Eq. (1) to prevent having under-reinforced cross sections whenever quotient A_g/A_{ch} tends to 1. Compliance with Eq. (1) and (2) is marked by underlining the corresponding ρ_x and ρ_y values in Table 1.

Salient features of the database are depicted in Fig. 2. Histograms of ρ_x and ρ_y indicate specimen volumetric transverse reinforcement ratios up to 2.5%, with typical values of approximately 0.5%, consistent with previous tests on square prisms (Scott et al. 1982; Moehle and Cavanagh 1985; Mander et al. 1988a). The slenderness ratio (h_u/b) histogram shows that all specimens can be regarded as slender with $h_u/b \geq 3.0$. The cross section aspect ratio (l_{be}/b) distribution is nearly uniform between 1.5 and 4.5, except for specimen P6 by Massone et al. (2014), which is close to square. The reinforcing bar slenderness ratio (s/d_b), where d_b is the nominal diameter of the longitudinal bars, correlates with the ability of transverse reinforcement to delay bar buckling. Monti and Nuti (1992) argued that a minimum value $s/d_b = 6$ is necessary to prevent bar buckling, which 82% of specimens in the database meet. However, specimens constructed with *Detail* 1 have some longitudinal bars only supported by the flexural stiffness of hoop legs and that are not engaged laterally

Table 1—As-tested material properties and reinforcement detailing

Au	ID	b, in.	l_{be}, in.	h_u, in.	c_c, in.	h_x, in.	f_c', ksi	f_{yt}, ksi	f_{yl}, ksi	N_b	ρ_l, %	d_{bt}, in.	N_{legX}	s, in.	ρ_x,* %	ρ_y,* %	D	H_{DZ}, in.
A	W1	8	24	48.0	1.5	9.6	4.4	72.5	69.6	10	2.3	0.50	3	2.7	1.05	2.95	1	22.7
A	W2	8	24	48.0	1.5	9.6	4.5	71.8	69.6	10	2.3	0.50	3	1.7	1.66	4.65	1	10
A	W3	12	36	72.0	1.5	10.3	3.8	72.2	68.8	14	2.55	0.50	4	4	0.59	1.09	1	21.7
A	W5	12	36	72.0	1.5	10.3	4	65	69.6	14	2.55	0.50	4	4	0.59	1.09	1	27.5
A	W6	12	36	72.0	1.5	7.8	4.2	65	67.9	18	2.51	0.50	5	4	0.74	1.09	1	25
A	W7	12	36	72.0	1.5	7.8	4.4	65	67.9	18	2.51	0.50	5	4	0.74	1.09	1	33
A	W8	12	36	72.0	1.5	7.8	4.4	71.5	76.4	18	2.51	0.50	5	4	0.74	1.09	1	30
A	W9	12	36	72.0	1.5	7.7	4.6	70.3	76.4	18	2.51	0.63	5	4	1.16	1.7	1	36.7
A	W10	12	36	72.0	1.5	7.8	4.7	71.5	76.4	10	1.39	0.50	5	4	0.74	1.09	2	32.5
A	W11	12	36	72.0	1.5	7.7	5.1	71.5	77.6	10	2.93	0.50	5	4	0.74	1.09	2	34
A	W12	12	36	72.0	1.5	7.6	4.4	70.3	77.6	10	2.93	0.63	5	4	1.16	1.7	2	32.5
M	P4	5.1	11.8	39.4	0.6	4.6	5.7	71.8	69.2	6	3.91	0.32	3	3.9	0.57	1.03	2	15.7
M	P5	7.1	11.8	39.4	0.6	4.6	5.7	71.8	69.2	6	2.83	0.32	3	3.9	0.57	0.69	2	15.7
M	P6	9.8	11.8	39.4	0.6	4.6	5.7	71.8	69.2	6	2.04	0.32	3	3.9	0.57	0.47	2	15.7
M	P12	7.1	11.8	63.0	0.6	4.6	5.7	71.8	69.2	6	2.83	0.32	3	3.9	0.57	0.69	2	15.7
M	P13	7.1	11.8	39.4	0.6	4.6	5.7	71.8	69.2	6	2.83	0.32	3	5.9	0.38	0.46	2	15.7
M	P14	7.1	11.8	39.4	0.6	4.6	5.7	71.8	69.2	6	2.83	0.32	3	5.9	0.38	0.46	2	15.7
M	P15	7.1	11.8	39.4	0.6	4.6	5.7	71.8	69.2	6	2.83	0.32	3	3.9	0.57	0.69	2	15.7
M	P17	7.1	11.8	39.4	0.6	4.6	5.7	47.9	69.2	6	2.83	0.32	3	5.9	0.38	0.46	2	15.7
M	P18	7.1	11.8	39.4	0.6	4.6	5.7	47.9	69.2	6	2.83	0.32	3	3.9	0.57	0.69	2	15.7
M	P20	7.1	11.8	39.4	0.6	4.6	5.7	71.8	69.2	6	2.83	0.32	2	3.9	0.38	0.69	1	15.7
M	P21	7.1	11.8	39.4	0.6	6.2	5.7	71.8	69.2	8	3.77	0.32	3	3.9	0.57	0.69	1	15.7
M	P22	7.1	11.8	39.4	0.6	6.2	5.7	71.8	69.2	8	3.77	0.32	3	3.9	0.57	0.69	1	15.7
M	P23	7.1	11.8	39.4	0.6	3.1	5.7	71.8	69.2	8	3.77	0.32	4	3.9	0.76	0.69	2	15.7
M	P24	7.1	11.8	39.4	0.6	3.1	5.7	71.8	69.2	8	3.77	0.32	4	3.9	0.76	0.69	2	15.7
W	CS9	8	15	40.0	0.8	6.1	4.3	68.9	82.4	10	2.56	0.38	4	5.0	0.65	0.65	1	19.8
W	CS15	8	15	40.0	0.8	6.1	4.1	68.9	82.5	10	2.56	0.38	3	2.5	0.98	1.31	1	12.9
JM	W2	5.9	27.6	15.4	1.0	3.5	4.1	49.3	47.9	16	1.72	0.24	8	1.0	1.39	2.26	3	15.7
JM	W3	5.9	27.6	15.4	1.0	3.5	4.1	45	47.9	16	1.72	0.24	14	2.0	1.22	1.13	3	15.7
JM	W5	5.9	27.6	15.4	1.0	3.5	4.1	45	47.9	16	1.72	0.24	8	2.8	0.48	0.79	3	15.7
JM	W6	5.9	27.6	15.4	1.0	3.5	4.1	47.9	47.9	16	1.72	0.39	8	1.7	2.3	3.74	3	15.7
JM	W9	5.9	27.6	15.4	1.0	3.5	5.9	49.3	47.9	16	1.72	0.24	8	1.0	1.39	2.26	3	15.7
JM	W10	5.9	27.6	15.4	1.0	3.5	5.9	49.3	42.1	16	3.06	0.24	8	1.0	1.39	2.26	3	15.7
JM	W11	5.9	27.6	15.4	1.0	3.5	5.9	49.3	42.1	16	3.06	0.24	8	2.0	0.7	1.13	3	15.7
JM	W12	5.9	27.6	15.4	1.0	3.5	5.9	52.2	42.1	16	3.06	0.39	8	1.7	2.3	3.74	3	15.7
JM	W13	5.9	27.6	15.4	1.0	6.1	5.9	52.2	42.1	10	1.08	0.39	5	1.2	2.01	5.24	2	15.7
JM	W14	5.9	27.6	15.4	1.0	6.2	5.9	49.3	42.1	10	1.08	0.24	5	1.2	0.72	1.88	2	15.7
T	1BM	4.3	9.4	23.6	0	4.3	3.5	52.6	50.3	10	3.06	0.16	3	3.1	0.2	0.29	1	6.5
T	2BM	4.3	9.4	23.6	0	2.2	3.5	52.6	50.3	10	3.06	0.16	6	3.1	0.4	0.29	3	5.5
T	3BM	4.4	9.5	23.6	0	2.2	3.5	52.9	50.3	10	2.9	0.24	6	3.1	0.88	0.63	3	4.5
T	4BM	4.4	9.5	23.6	0	2.2	3.5	52.9	50.3	10	2.9	0.24	6	2.4	1.17	0.84	3	6
T	5BM	4.3	9.4	23.6	0	4.2	3.5	52.6	47.1	10	7.82	0.16	3	3.1	0.2	0.29	1	8
T	1CM	2.7	14.5	23.6	0	5.5	3.5	52.6	50.3	12	3.77	0.16	4	2.8	0.2	0.53	1	8

Table 1 (cont.)—As-tested material properties and reinforcement detailing

Au	ID	b, in.	l_{be}, in.	h_u, in.	c_c, in.	h_x, in.	f_c', ksi	f_{yt}, ksi	f_{yl}, ksi	N_b	ρ_l, %	d_{bt}, in.	N_{legX}	s, in.	ρ_x,* %	ρ_y,* %	D	H_{DZ}, in.
T	3CM	2.8	14.4	23.6	0	2.7	3.5	52.9	50.3	12	3.57	0.24	6	1.6	1.16	1.96	2	5
MT	BZ1M	5.9	13	15.7	0.6	5.4	5.8	54.6	44.6	10	2.28	0.24	4	2.2	0.69	0.87	1	17
Median		7.1	15.0	39.4	0.8	4.6	4.7	65.0	69.2	10	2.83	0.32	4	3.9	0.72	1.03	—	15.7
Min.		2.7	9.4	15.4	0.0	2.2	3.5	45.0	42.1	6	1.08	0.16	2	1.0	0.20	0.29	—	4.5
Max.		12.0	36.0	72.0	1.5	10.3	5.9	72.5	82.5	18	7.82	0.63	14	5.9	2.30	5.24	—	36.7

*Underlined ρ_x and ρ_y values comply with Eq. (1) and (2).

Note: Au is Author [A is Arteta et al. (2014, 2015), M is Massone et al. (2014), W is Welt Welt et al. (2017), JM is Mander et al. (1988a), T is Taleb et al. (2016), and MT is Tripathi et al. (2020)]; c_c is clear cover of reinforcement; h_x is maximum center-to-center spacing of longitudinal bars laterally supported by corners of crossties or hoop legs; N_b is total number of longitudinal bars around the perimeter; ρ_l is ratio of total area of longitudinal steel; d_{bt} is nominal diameter of transverse reinforcement bar; N_{legX} is number of crossties or hoop legs ; ρ_y is volumetric transverse reinforcement ratio in short direction of section; D is *Detail* type. 1 in. = 25.4 mm; 1 ksi = 6.895 MPa.

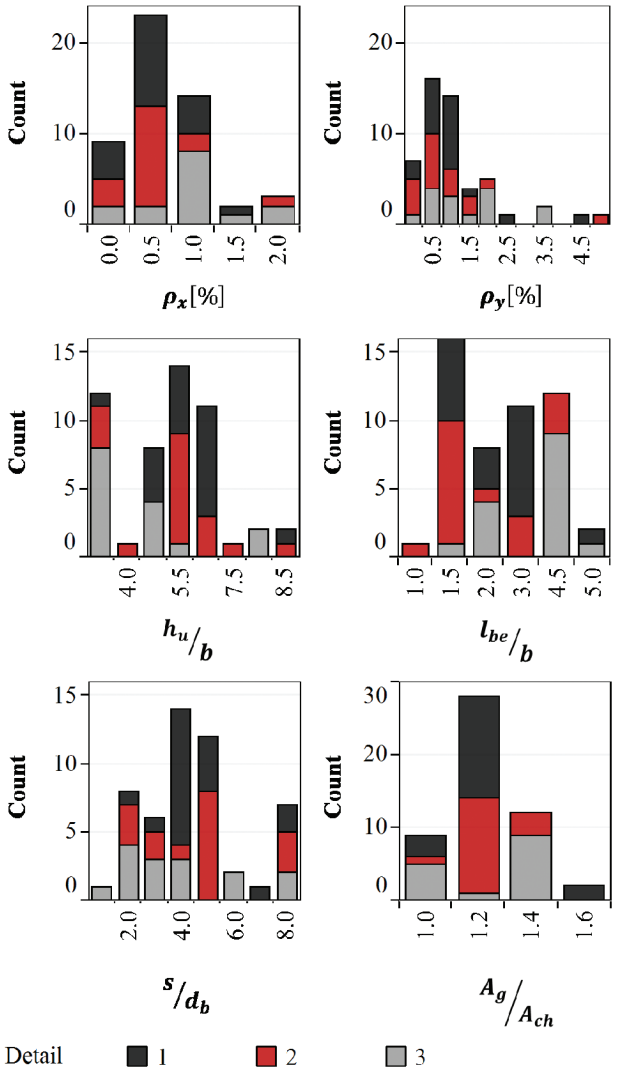

Fig. 2—Distribution of variables of interest discrimination by Detail *type: volumetric transverse reinforcement ratio, cross-section geometric parameters, and restraint ratio of longitudinal reinforcement.*

by a crosstie, hence the aforementioned conclusion may not apply to these specimens. In confined sections, a higher A_g/A_{ch} ratio leads to a greater expected loss in load-carrying capacity after cover spalling. A value of $A_g/A_{ch} = 1$ indicates no cover concrete, which is the case in approximately 15% of the specimens. The typical value is 1.2, corresponding to a cover-to-thickness ratio (c_c/b) of 9%.

EXPERIMENTAL FORCE-SHORTENING RELATIONSHIPS

The behavior of RC specimens under compression can be analyzed from three perspectives, illustrated in Fig. 3: (i) the overall average response; (ii) the behavior in the damaged zone (DZ); and (iii) the behavior in the undamaged zone (UDZ). The UDZ exhibits elastic behavior during testing, with minor or no loss of concrete cover or cracking, while the DZ region experiences strain softening after reaching peak stress. In the DZ of rectangular prisms, spalling of concrete cover, buckling of reinforcing bars, and crushing of the concrete core occur over a short height, as described by Arteta and Moehle (2023). The stress-strain curve in the DZ continuously softens, or decreases force capacity, for compressive straining in excess of the peak strength point (Jansen and Shah 1997). The UDZ, outside the localization zone, experiences an unloading curve starting from peak stress.

In this study, the force-shortening relationship within the DZ is determined using the hybrid model proposed by Arteta and Moehle (2023), as illustrated in Fig. 3(a). This model idealizes the specimens to behave as a system of two springs in series, with one spring representing the DZ and the other representing the UDZ. The following equilibrium and compatibility equations describe the system: $P = P_{UDZ} = P_{DZ}$ and $\delta = \delta_{UDZ} + \delta_{DZ}$; where P represents the axial force in the springs, δ represents the total shortening of the system, and δ_{UDZ} or δ_{DZ} represents the shortening of the corresponding spring.

The global response of the specimen can be represented by the relationship between the axial force P and the average strain $\varepsilon = \delta/h_u$. Similarly, the DZ response can be represented by the relationship between P and the average strain within the DZ, $\varepsilon_{DZ} = \delta_{DZ}/H_{DZ}$. It is worth emphasizing that, under a strain-softening regime, the local strain response depends on the gauge length (GL) over which strains are measured. Hence, the associated GL for the global and localized response is h_u and H_{DZ}, respectively. Figure 3(c) depicts an example of the contrasting behavior between the global (continuous black curve) and local (dashed red curve) responses of the uniaxial compression test W6 conducted by Arteta (2015).

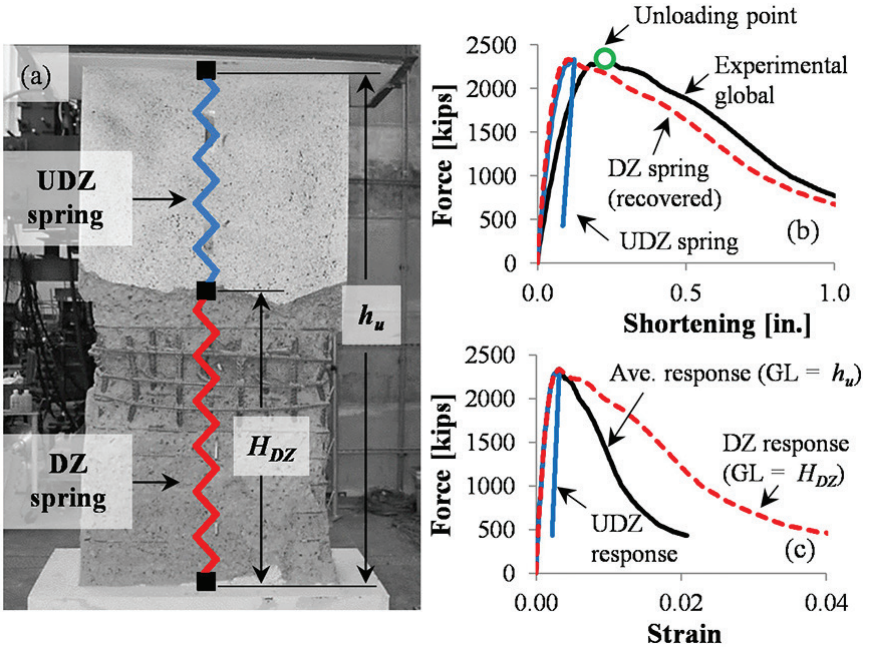

Fig. 3—Spring-in-series model of rectangular prims compression test (adapted from Arteta [2015]). (Note: 1 in. = 25.4 mm; 1 kip = 4.45 kN.)

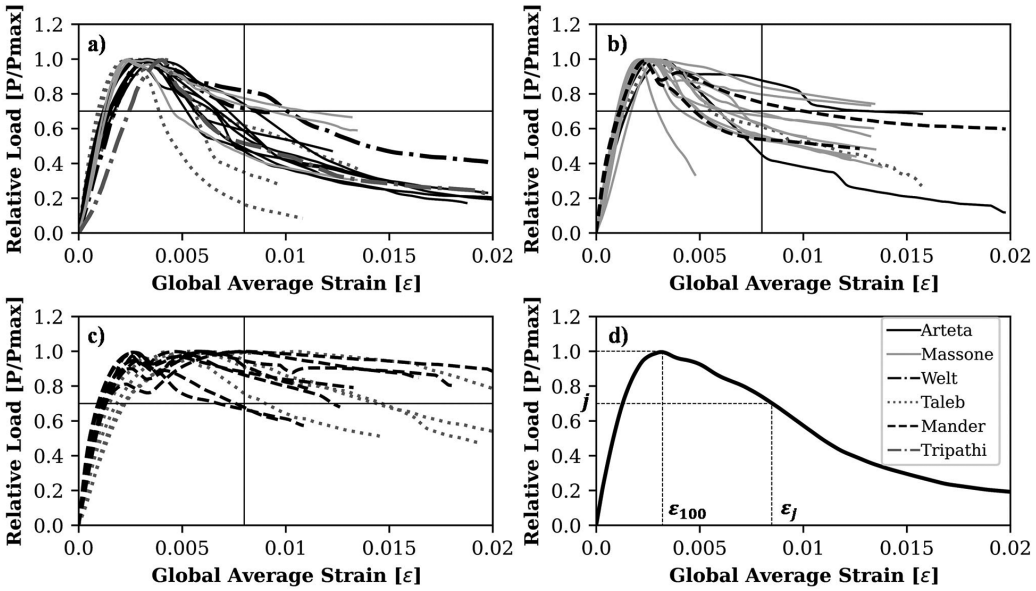

Fig. 4—Global relative force versus average strain curves organized by Detail *for specimens in the BEDB: (a)* Detail *1; (b)* Detail *2; (c)* Detail *3; and (d) definition of strength capacity level past peak force* j *and corresponding strain capacity* ε_j.

Global force-shortening relationship

Figures 4(a) to (c) present the relative force (P/P_{max}) versus the average strain of tests in the BEDB, classified by *Detail*. Figure 4(d) defines the strength capacity level past the peak force ($j = P_j/P_{max}$) on the descending branch of the curves, with a corresponding strain capacity ε_j. For example, $j = 0.8$ indicates a 20% drop in strength past the peak, with a corresponding strain capacity of ε_{80}. In Fig. 4(a) to (c), arbitrary reference horizontal and vertical lines are drawn at $j = 0.7$ and $\varepsilon = 0.008$, to help interpret the data. The fewer available data points above and to the right of the reference lines in the *Detail* 1 and 2 series compared to *Detail* 3 series are indicators of the larger ductility capacity of specimens constructed with the latter.

The data of average strain capacity at selected levels of j, aggregating all *Detail*, are fitted to a log-normal distribution with logarithmic mean (μ_{ln}) and standard deviation (σ_{ln}). These summary statistics serve to consider uncertainty in modeling walls dominated by flexural compression demand. The Kolmogorov-Smirnov (KS) (Massey 1951) and Anderson-Darling (AD) (Anderson and Darling 1952) tests for goodness-of-fit were employed to determine the significance of the fitted distribution. The null hypothesis of these tests is that "the sample distribution is log-normal." The null hypothesis is rejected statistically when the p-value is lower than the chosen significance level. The null hypothesis is not rejected at a 5% significance level for j values of 0.9, 0.8 and 0.7, and at a 1% significance level for the strain at peak

Table 2—Summary statistics of strain at various strength levels past peak considering detail type

Summary	*Detail* 1				*Detail* 2				*Detail* 3			
Statistics	ε_{100}	ε_{90}	ε_{80}	ε_{70}	ε_{100}	ε_{90}	ε_{80}	ε_{70}	ε_{100}	ε_{90}	ε_{80}	ε_{70}
P5	0.0023	0.0036	0.0040	0.0044	0.0021	0.0027	0.0032	0.0037	0.0028	0.0034	0.0052	0.0070
P95	0.0040	0.0054	0.0075	0.0102	0.0031	0.0067	0.0100	0.0112	0.0093	0.0181	0.0202	0.0203
Mean	0.0030	0.0045	0.0057	0.0068	0.0026	0.0041	0.0055	0.0064	0.0057	0.0094	0.0125	0.0125
Median	0.0029	0.0045	0.0053	0.0065	0.0025	0.0040	0.0050	0.0059	0.0059	0.0080	0.0118	0.0123
Std. Dev.	0.0006	0.0006	0.0013	0.0020	0.0003	0.0013	0.0022	0.0026	0.0024	0.0050	0.0054	0.0055
CV	19%	14%	22%	29%	13%	32%	40%	41%	42%	53%	43%	44%
μ_{ln}	–5.829	–5.406	–5.194	–5.031	–5.974	–5.541	–5.277	–5.123	–5.261	–4.798	–4.477	–4.465
σ_{ln}	0.18	0.14	0.22	0.29	0.13	0.30	0.37	0.36	0.44	0.54	0.48	0.43
		ε_{DZ90}	ε_{DZ80}	ε_{DZ70}		ε_{DZ90}	ε_{DZ80}	ε_{DZ70}		ε_{DZ90}	ε_{DZ80}	ε_{DZ70}
P5		0.0047	0.0063	0.0071		0.0031	0.0044	0.0057		0.0044	0.0094	0.0148
P95		0.0089	0.0145	0.0202		0.0125	0.0197	0.0251		0.0436	0.0470	0.0547
Mean		0.0071	0.0102	0.0134		0.0062	0.0096	0.0118		0.0214	0.0281	0.0339
Median		0.0073	0.0103	0.0129		0.0054	0.0079	0.0098		0.0169	0.0288	0.0310
Std. Dev.		0.0015	0.0027	0.0046		0.0030	0.0053	0.0064		0.0141	0.0133	0.0167
CV		22%	27%	34%		49%	55%	54%		66%	47%	49%
μ_{ln}		–4.977	–4.626	–4.371		–5.185	–4.778	–4.553		–4.069	–3.705	–3.504
σ_{ln}		0.23	0.28	0.36		0.45	0.52	0.48		0.76	0.59	0.54

Note: Std. Dev. is standard deviation.

strength. The parameters of the distribution (μ_{ln}, σ_{ln}) are: (–5.725, 0.38), (–5.291, 0.45), (–5.032, 0.48), (–4.960, 0.41) for j = 1, 0.9, 0.8, and 0.7, respectively.

Table 2 provides additional summary statistics, such as the fifth and 95th percentiles (P5 and P95, respectively), mean, median, standard deviation, coefficient of variation (CV), for each *Detail* and global strain capacity level ε_{100}, ε_{90}, ε_{80}, and ε_{70}. Although mean values for *Detail* 1 and 2 are similar, the upper-bound strains (ε_{90}, ε_{80}, and ε_{70}) for *Detail* 2 are higher. Note that the mean strain capacities of specimens in *Detail* 3 are approximately double those in *Detail* 1 and 2. As discussed earlier, the *Detail* is just one of the important parameters affecting the ductility capacity. Variability in the experimental results shown in Fig. 4(a) to (c) can be attributed to other important parameters that are explored in detail in the following sections.

Damaged zone extension

The length of the damaged zone (H_{DZ}) in a compression test is associated with the localization process and affects the specimen fracture energy in compression. In concrete cylinders, the H_{DZ} is influenced by the maximum aggregate size, the average distance between aggregates, and the compressive strength (Nakamura and Higai 1999). In RC prisms tested under uniform compression, the transverse reinforcement layout impacts modestly the H_{DZ} (Arteta and Moehle 2023).

In this paper, the H_{DZ} represents an equivalent length where inelastic deformations are concentrated. The length of the damaged zone reported in Table 1 was either obtained by reports in the literature or measured from post-test photographs within the scope of this article. Figure 5(a) presents the relative distribution of H_{DZ} normalized by the specimen thickness (H_{DZ}/b) for specimens in the BEDB. Consistent with post-earthquake reconnaissance reports (Wallace et al. 2012) and recent experiments on relatively thin walls (Segura and Wallace 2018a,b), plasticity typically concentrates over a height between 2.0 and 2.5 times the thickness of the specimens. Note that there is no apparent trend with *Detail*. Further, consistent with observations by Nakamura and Higai (1999) and Jansen and Shah (1997) in concrete cylinders of different height and aspect ratio, Fig. 5(b) and (c) show there is no apparent trend of H_{DZ}/b with the specimen aspect ratio.

Damaged zone force-shortening relationship

The response within the DZ can be approximated from the global force-shortening relationship by distributing the total shortening δ between the two springs in Fig. 3(a). Up to the peak load δ is distributed between δ_{DZ} and δ_{UDZ} in proportion to the inverse of the spring length, $1/H_{DZ}$ and $1/(h_u - H_{DZ})$, for the DZ and UDZ spring, respectively. Beyond the peak load, at each level j, the displacement in the DZ spring is calculated as $\delta_{DZ} = \delta - \delta_{UDZ}$. Note that beyond the peak load, the UDZ spring is unloading with stiffness $K_{UDZ0} = 1/(h_u - H_{DZ})[E_c(A_g - A_s) + E_sA_s]$, where A_s is the total area of longitudinal steel, and E_s and E_c are the reinforcing steel and concrete Young's modulus. Figure 3(b) illustrates the process.

The average strain in the DZ is calculated by normalizing its shortening by the H_{DZ}, $\varepsilon_{DZ} = \delta_{DZ}/H_{DZ}$. This method was applied to all specimens in Table 1, except for those by Massone et al. (2014) and Mander et al. (1988a), who measured the displacements directly from a pre-defined DZ length. Therefore, the global average curves were calculated

from the DZ curves using an inverse estimation method for their specimens. Table 2 provides the ε_{DZ} values recovered for the tests in the BEDB, classified by *Detail*. Considering all *Detail* type, the mean DZ strain capacities are between 1.5 and 2.7 times greater than the mean average (global) strain. A linear trend of the form $\varepsilon_{DZj} = m\varepsilon_j + c$ fits the average versus DZ strains relationship, with a correlation coefficient $r \geq 0.91$. The slopes and intercepts (m, c) for j = 0.9, 0.8, and 0.7 are (2.80, –0.005), (2.80, –0.005), and (2.97, –0.006), respectively. This simple model serves to project average strains to DZ strains, or vice versa, depending on the data available.

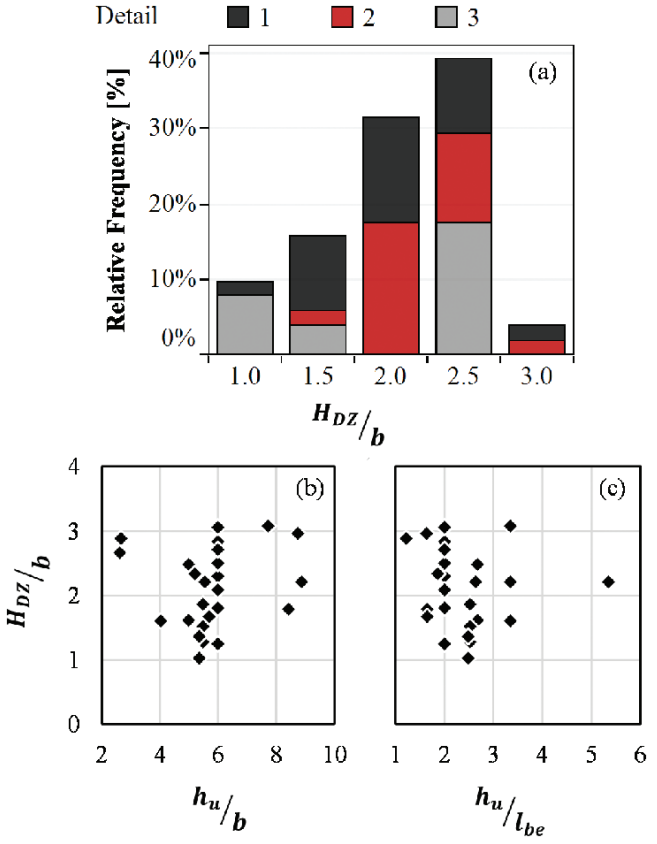

Fig. 5—Histogram of normalized damaged zone length (H_{DZ}/b) for specimens in BEDB.

Absorbed energy

The absorbed energy (E_A) is defined as the amount of energy needed to load a specimen from zero to the final shortening value. For the damaged zone, this value is calculated as the area under the force-shortening curve, $E_A = \int P d\delta_{DZ}$. The total E_A is determined for the specimens in the BEDB, up to j = 0.2 (when available), as follows: $E_A = \int_0 P d\delta_{DZ} = H_{DZ} \int_0 P d\varepsilon_{DZ}$. With the factorization of H_{DZ}, this equation indicates that specimens that can sustain the axial load through larger strains and over a greater damaged region will absorb more energy. The absorbed energy values are normalized to make comparisons easier, given that the axial load capacity varies from one specimen to another. The selected normalization factor is the work required to load a specimen of height 2.5b, which is a typical damaged zone length, from zero force to the nominal compression capacity P_o at an average strain of 0.002—that is, $G_E = 1/2[P_o(0.002 \cdot 2.5b)]$, where $P_o = 0.85f_c'(A_g - A_s) + A_s f_y$.

Figures 6(a) to (c) show the trend of the normalized absorbed energy of the specimens at different levels of strength loss past the peak axial force (that is, $400E_{Aj}/P_o b$, where E_{Aj} is the post-peak absorbed energy up to strength level j). As anticipated, specimens with *Detail* 3 exhibit a larger slope of normalized E_{Aj} values than those with *Detail* 1 and 2. This difference is due to the improved transverse reinforcement detailing in *Detail* 3 specimens. The measured E_{Aj} values in the DZ support the classification by *Detail* type, which categorizes specimens based on their transverse reinforcement layout. For example, the [min, median, max] values of normalized E_{Aj} calculated for j = 0.7 are [1.96, 5.07, 6.6], [1.26, 4.03, 10.76], [5.5, 9.5, 27.9] for specimens with *Detail* 1, 2 and 3, respectively (Fig. 6(d)). Note the broader range of normalized E_{Aj} exhibited by the *Detail* 2 group compared to the *Detail* 1 group, reaching maximum normalized E_{Aj} values greater than 16 for j = 0.6 (Fig. 6(b)). The lower-bound values in *Detail* 2 are smaller than those in *Detail* 1 due to lower confinement levels in some specimens in the former group.

REGULARIZED POST-PEAK COMPRESSION MODEL

The compressive strain capacity of reinforced concrete prisms is affected by various factors, such as the amount

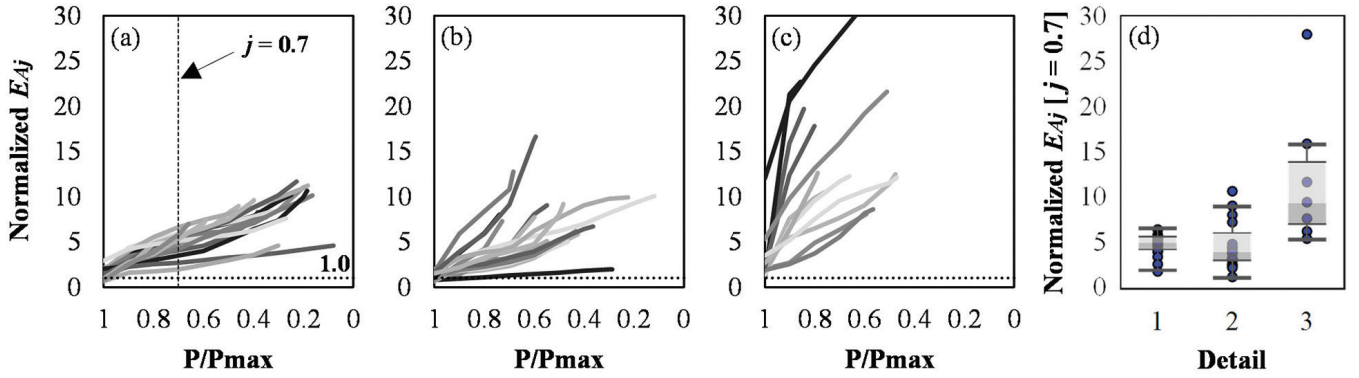

Fig. 6—Normalized post-peak absorbed energy (E_{Aj}) for: (a) Detail *1; (b)* Detail *2; and (c)* Detail *3; and (d) distribution of normalized E_{Aj} for j = 0.7.*

and arrangement of transverse reinforcement, and the gauge length used for measurement (Shah and Sankar 1987; Bažant 1989; Arteta and Moehle 2023). The plastic strains reported so far were calculated from displacements measured over a range of gauge lengths. However, the non-uniform strain distribution resulting from damage localization along the specimen length highlights the need to associate reported plastic strains with an appropriate gauge length to accurately interpret the results (Markeset and Hillerborg 1995).

The next step is to present a compression backbone model for the force-strain capacity curve of the damaged zone, considering the height of damage localization. The model will be associated with the specimen cross-section geometry and the longitudinal and transverse reinforcement detailing. The user is expected to provide the anticipated or desired plastic hinge length over which values of ε_{DZj} are to be modeled for four discrete strength levels, $j = [1, 0.9, 0.8, 0.7]$. A mechanical fracture energy model supports the stochastic analysis to constrain the extrapolation capabilities.

Modified Compressive Fracture Energy (MCFE)

The compressive fracture energy is defined as the energy per cross-sectional area absorbed in the damaged zone, $G_{fc} = E_A$/A. Variable G_{fc} can be used as a mesh-independent parameter to define the post-peak (that is, softening) branch for concrete specimens for a user-desired plastic hinge length (Coleman and Spacone 2001; Marafi et al. 2019). Jansen and Shah (1997) defined the post-peak concrete crushing energy as the area under the softening portion of the compression stress-shortening curve, expressed as $G_{fc} = \int \sigma d\delta_{inel}$, where σ is the concrete stress, and δ_{inel} is the inelastic post-peak shortening of the cylinder. The G_{fc} remains constant regardless of specimen size. If the inelastic displacement of the localized region is independent of its length, the post-peak fracture energy equation can be written as $G_{fc} = H_{DZ} \int \sigma d\varepsilon_{inel}$, where ε_{inel} is the inelastic post-peak strain within the damaged zone.

The area of interest is shaded in Fig. 7. A similar model was employed by Coleman and Spacone (2001) to present the impact of the fracture energy in compression in modeling the softening response of concrete structural members using a force-based finite element formulation. Their backbone was a simplified version of the Kent and Park (1971) concrete stress-strain curve, which has a parabolic ascending branch, followed by a simplified linear post-peak branch with negative slope. Here, it is adapted to represent the Modified Compressive Fracture Energy (MCFE, G_{fc}^*) for the rectangular prisms of the BEDB. The MCFE is the local post-peak absorbed energy per unit area in the damaged region

$$G_{fc}^* = \int \sigma^* d\delta_{DZ} \tag{3}$$

where the modified stress, σ^*, is defined as the measured axial load divided by the cross-sectional area (P/A). The normalizing area A may be chosen as A_{ch}, if the post-peak axial force acts on a reduced cross-sectional area due to cover spalling. Although the cover area is not lost instantly at peak load, as Arteta and Moehle (2023) described, this simplification aids in constructing the subsequent semi-empirical stochastic model. Nevertheless, this decision is not critical in the model development because the normalizing area cancels out later in the formulation.

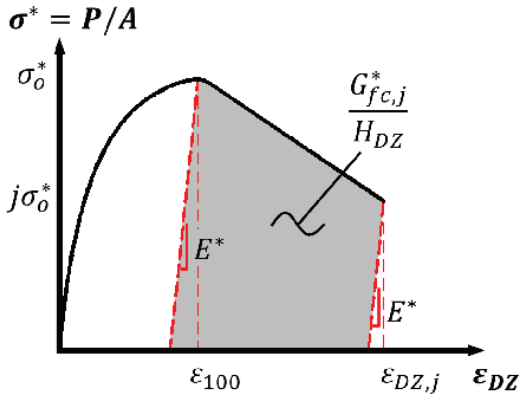

Fig. 7—Modified stress versus damaged zone strain backbone model for prisms in compression with definition of MCFE through strength level j.

Considering the inelastic shortening of the prisms is independent of the damaged zone length, Eq. (3) can be recast to estimate the MCFE through strength level j past the peak as

$$G_{fc,j}^* = H_{DZ} \int \sigma^* d\varepsilon_{DZ} = \frac{H_{DZ}}{A} \int P d\varepsilon_{DZ} = \frac{E_{Aj}}{A} \tag{4}$$

Figure 7 illustrates the simplified σ^* versus ε_{DZ} model that serves as a backbone to the stochastic model presented herein. The goal is to estimate strain capacity level $\varepsilon_{DZ,j}$ from the strain at peak ε_{100}, recognizing the shaded area is equal to ${G_{fc,j}}^*/H_{DZ}$

$$\varepsilon_{DZ,j}^* = \frac{2\,G_{fc,j}^*}{(1+j)\,\sigma_o^*\,H_{DZ}} - \frac{(1-j)\,\sigma_o^*}{E^*} + \varepsilon_{100} \tag{5}$$

where E^* is the weighted modulus of elasticity of the prism cross section; and ${\sigma_o}^*$ is the peak modified stress.

Equation (5) allows projection of the damaged zone strain at peak load along the downward slope, while keeping the compressive response of the specimen independent of mesh size by treating the damaged zone length as a variable. Equation (6) approximates Eq. (5) by eliminating the addition and subtraction of the triangular areas bounded by E^*, while incurring an error of less than 2% in the measured fracture energy. Henceforth, Eq. (6) will be used to fit the stochastic model for each *Detail* and value of j

$$\varepsilon_{DZ,\,j}^* = \varepsilon_{100} + \frac{2\,G_{fc,j}^*}{(1+j)\,\sigma_o^*\,H_{DZ}} \tag{6}$$

Stochastic parameter estimation

Parameters ${\sigma_o}^*$, $\varepsilon_{100,}$ and ${G_{fc,j}}^*$ in Eq. (6) are not readily available to the user beforehand. Thus, a predictive model is presented next for their estimation. Parameter ${\sigma_o}^*$ is linked to the compressive strength of the rectangular cross section and can be determined by fitting empirical data after isolating specimens affected by excessive out-of-plane eccentricity. This required constructing an axial force (P), bending moment (M) interaction diagram for each cross section

using as-tested material properties, with the moment direction of interest being the one compressing the cross-section side with length l_{be}. Normalized eccentricity values (e/b) are estimated by intersecting the PM orbit with the experimental peak load, P_{max}, and obtaining the corresponding moment capacity, M. Deviations of P_{max} from P_o are attributed mainly to eccentricity (Arteta and Moehle 2023), and corresponding values $e = M/P_{max}$ are expected to increase as P_{max}/P_o decreases. A linear trend was fitted for estimating σ_o* with P_o/A as a proxy from data complying with an eccentricity threshold below 5%. The linear fit has an intercept forced to zero, with a statistically significant slope (p-value < 0.0001), resulting in an r of 0.99. Given the material properties, cross-sectional geometry, and longitudinal steel area, the analyst can estimate the modified peak strength with Eq. (7)

$$\sigma_o^* = 1.1\frac{P_o}{A} \tag{7}$$

Results in Table 2 indicate that parameter ε_{100} varies within a modest range for *Detail* 1 and 2, which have similar mean and median values. The CV of the aggregated data is 18%, indicating moderate homogeneity, as rated by Rustom (2012). Conversely, ε_{100} values for *Detail* 3 have a CV > 40%. The data supports selecting a single model for *Detail* types 1 and 2 (Fig. 8), and another for *Detail* 3 (Fig. 8). The predictive variable η in Eq. (8) encapsulates information regarding the through-thickness direction of the cross-section geometry, transverse reinforcement, and material properties. It correlates with the strain at peak strength through the linear models in Eq. (9) and (10) (p-value < 0.0001), which help predicting $\varepsilon_{100,1\&2}$ and $\varepsilon_{100,3}$, respectively

$$\eta = \rho_x \frac{b}{d_{bt}}\frac{f_{yt}}{f_c'} \tag{8}$$

$$\varepsilon_{100,1\&2} = 0.0002\eta + 0.0022 \le 0.004 \tag{9}$$

$$\varepsilon_{100,3} = (0.0056\eta - 0.0057) \begin{matrix} \ge \varepsilon_{100,1\&2} \\ \le 0.02 \end{matrix} \tag{10}$$

The normalized post-peak MCFE is defined for each strength level j as $G_{fc,j}^*/G_E$. Normalization by the elastic energy G_E enables the comparison and modeling of specimens with different strength. Variable ρ_x is selected as a proxy for estimating $G_{fc,j}^*/G_E$. It exhibits a strong linear correlation with the MCFE for *Detail* 2 and 3, although the trend is not discernible for *Detail* 1 as shown in Fig. 9(a). For *Detail* 2 and 3, the intercept is not statistically significant, hence set to zero (Fig. 9(b)). The linear trends in Fig. 9(b) exhibit an r in the range 0.88 to 0.98, and the slopes $B_{1,2j}$ and $B_{1,3j}$ are statistically significant with p-value < 0.0001. Equation (11) shows the functional form of the linear trend for estimating $G_{fc,dj}^*$ for each *Detail* d, and strength level j. Intercepts $B_{0,dj}$ and slopes $B_{1,dj}$ are summarized in Table 3. Note the post-peak MCFE for *Detail* 1 is set constant, equal to the mean value of all specimens. The restriction in Eq. (11) imposes a lower bound to *Detail* 2 and 3 to prevent having fracture energies smaller than that of *Detail* 1 when ρ_x falls below a certain limit. Notably,

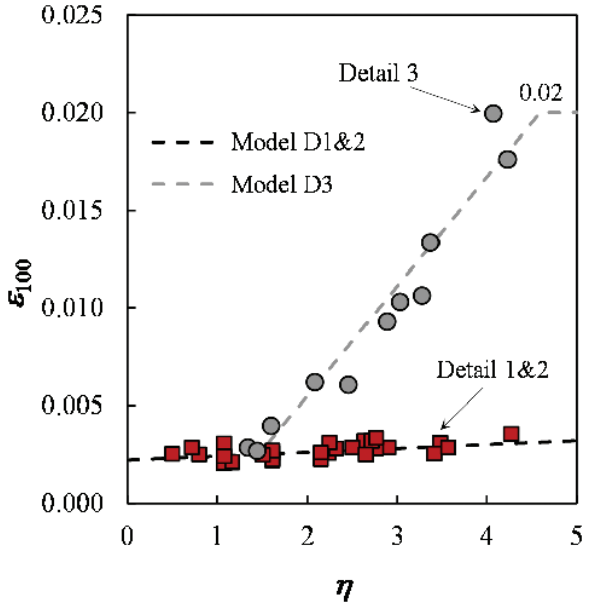

Fig. 8—Linear fit for scattergram of strain at peak strength versus η *for* Detail *1, 2, and 3.*

this restriction indicates that minimum MCFE for any *Detail* at a 20% strength loss past the peak—that is, for $j = 0.8$—is approximately $5G_E \sim 0.013P_o b$

$$G_{fc\,d,j}^* = [B_{0,dj} + B_{1,dj}\rho_x]\,G_E^* = 0.0025\,[B_{0,dj} + B_{1,dj}\rho_x]\frac{P_o}{A}b \tag{11}$$

with $[B_{0,dj} + B_{1,dj}\rho_x] \ge B_{0,1j}$.

Post-peak strain model

One simplification assumed previously is that one can estimate $\varepsilon_{DZ,j}$ from ε_{100} using a straight line (Eq. (6)). However, the experimental data in Fig. 4 show the path between ε_{100} and $\varepsilon_{DZ,j}$ is not necessarily linear. Hence, a correction between the model estimate ($\varepsilon_{DZ,dj}^*$) and the measurements ($\varepsilon_{DZ,dj}$) is defined by Eq. (12), with a correlation coefficient, $r > 0.98$, for any *Detail*. Considering all j levels, coefficient A_1 varies between 0.95 and 1.00 for *Detail* 1 and 2, and between 0.60 and 0.95 for *Detail* 3

$$\varepsilon_{DZ,dj} = A_{1,dj}\,\varepsilon_{DZ,dj}^* \tag{12}$$

The model for the post-peak damaged-zone strain, $\varepsilon_{DZ,dj}$, as a function of H_{DZ} is formulated in Eq. (13) by substituting Eq. (6) into (12), along with the proxies for σ_o^*, and $G_{fc,j}^*$ formulated in Eq. (7) and (11), respectively. The resulting model is a function of the volumetric transverse reinforcement ratio in the through-thickness direction, ρ_x, the specimen cross-sectional width b, and the expected plastic hinge length H_{DZ}. This allows for the adjustment of the post-peak strain capacity as a function of the damaged zone length selected by the modeler. As H_{DZ} decreases, $\varepsilon_{DZ,dj}$ will increase, and vice versa, which is known as the auto regularization capability of the model. As anticipated previously, the model is not a function of the specimen cross-sectional area.

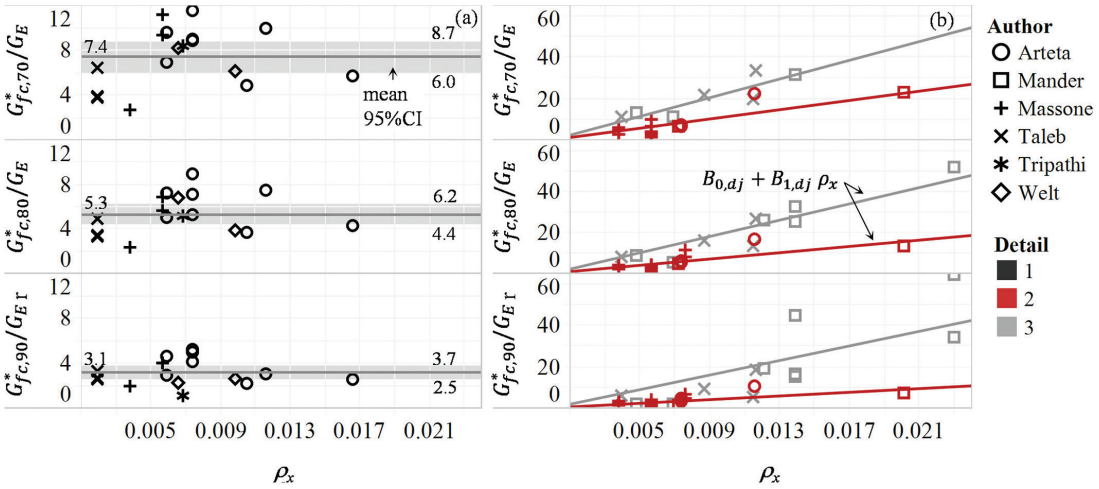

Fig. 9—Post-peak MCFE model for: (a) Detail *1; and (b)* Detail *2 and 3.*

Table 3—Coefficients of modified fracture energy model

Strength level j	$B_{0,1j}$	$B_{1,2j}$	$B_{1,3j}$
0.9	3.1	445	1760
0.8	5.3	770	1990
0.7	7.4	1120	2260

Note: $B_{1,1j} = B_{0,2j} = B_{0,3j} = 0$.

Table 4—Correction coefficients of post-peak strain model

Strength level j	$A_{1,1j} \cdot D_{1,1j}$	$A_{1,2j} \cdot D_{1,2j}$	$A_{1,3j} \cdot D_{1,3j}$
0.9	1.05	0.90	0.60
0.8	1.10	0.90	0.80
0.7	1.10	0.90	0.90

It should be noted that while strength influences the post-peak response in plain concrete (Shah and Sankar 1987; Wee et al. 1996), factors such as buckling length and the extent of plasticity are also influential but challenging to quantify individually. Hence, this work posits that the post-peak response in reinforced concrete is predominantly governed by the plastic hinge length within the limited strength range of the BEDB ($3.5 \le f_c' \le 5.9$ ksi)

$$\varepsilon_{DZ,d_j} = A_{1,d_j} \cdot D_{1,dj} \left(\varepsilon_{100,d} + \frac{[B_{0,dj} + B_{1,dj}\rho_x]\, b}{220\,(1+j)\,H_{DZ}} \right) \quad (13)$$

In Eq. (13), the user can either plug-in the ε_{100} model in Eq. (9) and (10), or their best estimate for the strain at peak strength based on their knowledge of the plain concrete properties. A second correction factor, D_1, addresses the errors that accumulate when estimating the parameter values of interest due to their stochastic nature. Factor D_1 is also linear with a correlation coefficient, $r > 0.88$, for any *Detail*. The product $A_{1,dj} \cdot D_{1,dj}$ for *Detail d* and strength level j is summarized in Table 4.

MODEL PERFORMANCE

Figure 10 compares the linear post-peak strain capacity model in Eq. (13) against experimental data. Individual markers represent the model results for ε_{100} through $\varepsilon_{DZ,70}$ along with a linear fit that passes through ε_{100}. Solid lines correspond to estimates for a plastic region height (L_p) equal to the experimental damaged zone height in Table 1, while dotted and dashed lines correspond to one-half and twice that length, respectively. The rotation of the post-peak linear model demonstrates its auto regularization capabilities. Thus, a single cross section can have several force-strain relationships, depending on the height at which the modeler expects the plasticity to concentrate, providing a mesh-independent procedure for nonlinear structural modeling that provides consistent force-deformation results.

The post-peak model residuals are calculated as the difference between the measured strain and the model estimate, $\varepsilon_{DZ} - \overline{\varepsilon}_{DZ}$, indicating overpredictions of the model for negative residuals. Parameters ρ_x, b, and H_{DZ} plugged in Eq. (13) are the experimental ones summarized in Table 1. Figure 11 shows the residuals versus *Detail*, strength level and prediction variables ρ_x and H_{DZ}/b. The results show that the model fits the data with no apparent bias.

FORCE-STRAIN MODEL

The ascending branch of the experiments is modeled using Eq. (14) through (16), which specializes the functional form for the stress-strain relationship of confined concrete from Mander et al. (1988b), to a force-strain relationships of reinforced concrete prisms. Figure 12 shows the model estimates, including the ascending branch and the post-peak response considering the experimental damaged zone height (for example, $L_p = H_{DZ}$), for each of the 45 experimental tests included in the BEDB. The results show a good agreement between the model and the experiments for all *Detail*. The contrasting response between specimens with *Detail* 1 and 2, and those with *Detail* 3 is captured adequately

$$\frac{P}{P_{max}} = \frac{\left(\frac{\varepsilon_{DZ}}{\varepsilon_{100}}\right) r}{r - 1 + \left(\frac{\varepsilon_{DZ}}{\varepsilon_{100}}\right)^r} \quad (14)$$

$$r = \frac{EA_{BE}}{EA_{BE} - \frac{P_o}{\varepsilon_{100}}} \quad (15)$$

$$EA_{BE} = E_c(A_g - A_s) + E_s A_s \quad (16)$$

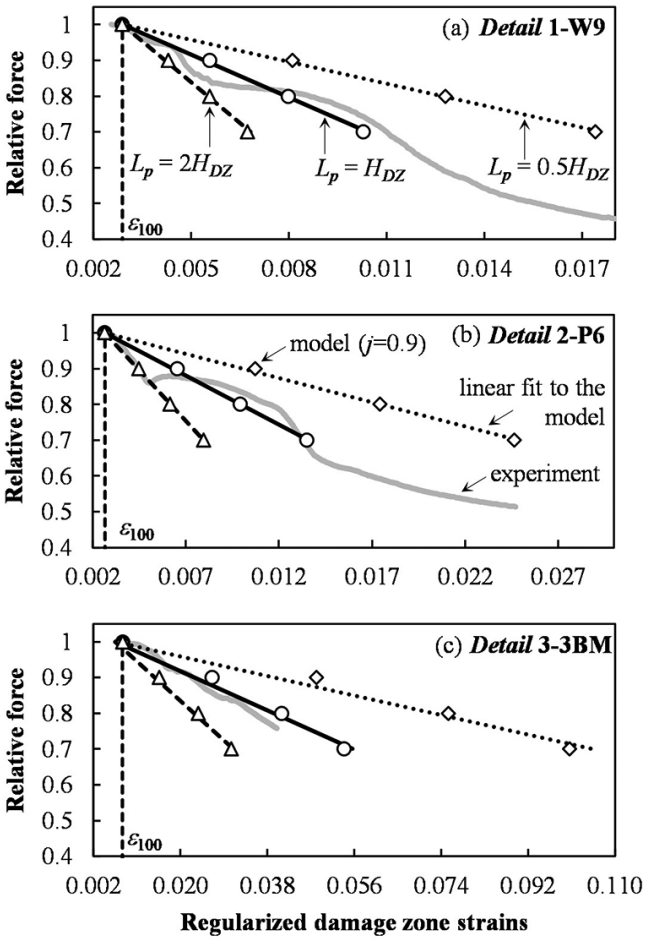

Fig. 10—Post-peak model autoregularization capabilities. Model and experiment comparison examples for: (a) Detail *1; (b)* Detail *2; and* Detail *3.*

SUMMARY AND USER GUIDANCE

This paper presents an analytical model to estimate the compressive force-deformation response of rectangular reinforced concrete (RC) prisms representing the compression zone of earthquake-resistant structural walls. The model predicts the compressive behavior for both ACI 318-compliant and non-compliant wall boundary elements considering a wide range in the quantity and layout of transverse and longitudinal reinforcement. The model uses force, strain, and fracture energy values derived from 45 laboratory tests on boundary element specimens to provide a mesh-independent procedure that adjusts the post-peak strain response to account for the user input plastic length, a process termed "autoregularization" herein. The following observations and conclusions are made:

1. The compressive force-strain relationship accounts for the variables that contribute most to stable compressive behavior of a structural wall boundary element, including the through-thickness transverse reinforcement ratio, and the cross-sectional width.

2. The model appropriately captures the superior compressive force-strain relationship observed in laboratory tests for RC sections with ACI 318-compliant transverse reinforcement ratios provided by overlapping hoops, demonstrated by a larger peak compressive strain and a shallower post-peak slope.

3. The model applies an autoregularization technique to provide mesh-independent results, enabling users to select the desired structural modeling discretization (for example, plastic hinge length), while obtaining consistent structural modeling results.

Future research is recommended to apply the compressive force-strain relationship in nonlinear structural models of structural walls tested in the laboratory, investigating the implications of the novel modified compression fracture energy (MCFE) model. It is suggested that both ACI 318-compliant and non-compliant walls be included in this investigation.

User guidance: Parameter $\varepsilon_{DZ,dj}$ in Eq. (13) is the post-peak strain capacity of a rectangular prism with *Detail* type

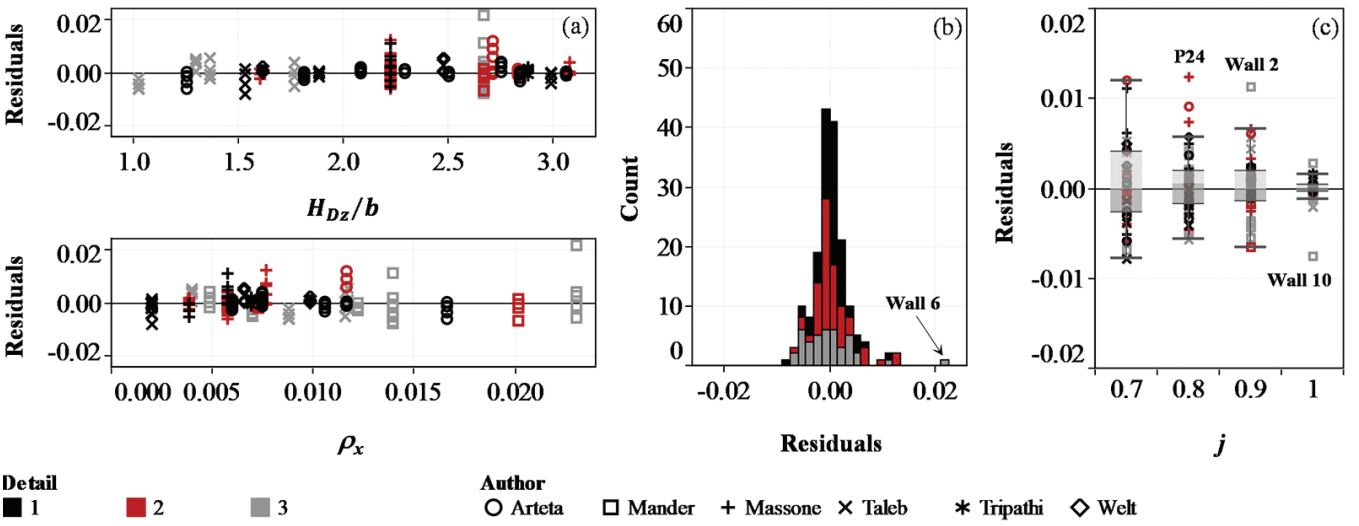

Fig. 11—Post-peak model residuals: (a) trend with specimen aspect ratio and volumetric transverse reinforcement ratio; (b) distribution by Detail*; and (c) distribution by strength level.*

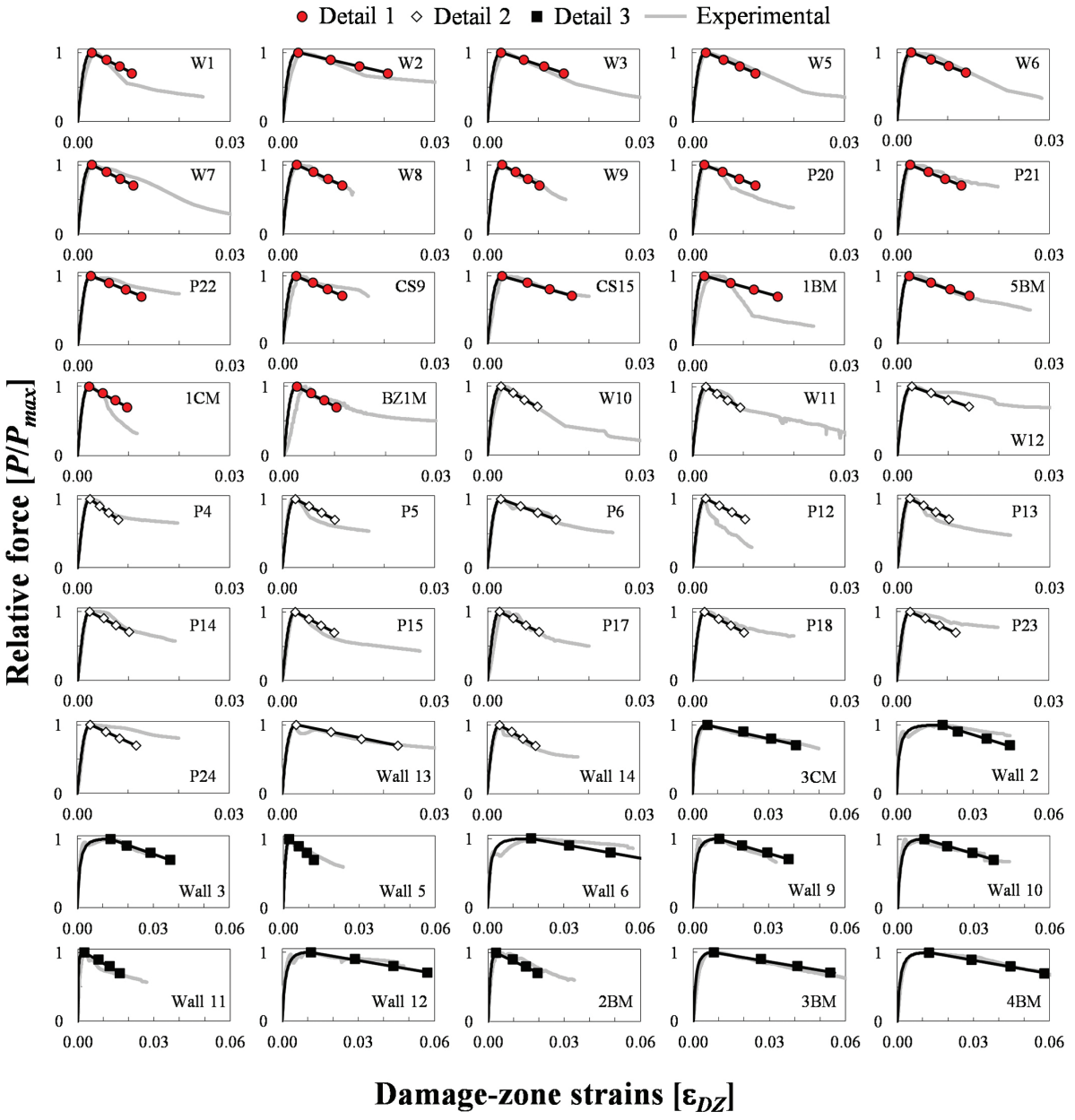

Fig. 12—Model and experimental data comparison.

d, at a strength level $j = P/P_{max}$ beyond the peak, assumed to occur over a plastic hinge length $L_p = H_{DZ}$, which is selected by the user. The relative force-strain ascending branch is modeled up to $\varepsilon_{100,d}$ with Eq. (14) through (16). A post-peak linear branch can be constructed by fitting a linear trend through points ($\varepsilon_{DZ,d90}$, $j = 0.9$), ($\varepsilon_{DZ,d80}$, $j = 0.8$), and ($\varepsilon_{DZ,d70}$, $j = 0.7$), forced to pass through the peak strength and corresponding strain ($\varepsilon_{100,d}$, $j = 1$), calculated with Eq. (9) and (10). If the total force is required, the relative force values may be scaled by $1.1P_o$ (refer to Eq. (7)).

To use the autoregularization capabilities correctly, an L_p value within an acceptable range must be entered. While ASCE/SEI 41 (2017) specifies that L_p should be the lesser of one-half the flexural depth of the wall and one story height, post-earthquake reconnaissance experiences and experimental tests on relatively thin RC walls indicate that damage tends to concentrate in a smaller portion, suggesting L_p can be related to the wall thickness, b. Typical values are between $2b \le L_p \le 3b$, which agrees with 77% of the results in the BEDB. It is recommended that L_p values within this range be used to use the force-deformation model adjusted in this study. Notably, Takahashi et al. (2013) proposed a plastic hinge model for a wall under ultimate flexural compression demand compatible with these recommendations, as explained by Arteta and Moehle (2023).

AUTHOR BIOS

ACI member **Carlos A. Arteta** *is Associate Professor of Civil Engineering at Universidad del Norte, Barranquilla, Colombia. He is a member of ACI Committees 318, Structural Concrete Building Code, and 374, Performance-Based Seismic Design of Concrete Buildings. His research interests include response and design of buildings to earthquake actions, with emphasis in analysis, design, and risk evaluation of reinforced concrete structural systems.*

Jefferson Piedrahita *is an Instructor Professor of Civil Engineering at Universidad Tecnológica de Bolívar, Cartagena de Indias, Colombia. His*

research interests include seismic response, design, and analysis of buildings, specifically reinforced concrete structural system.

ACI member **Christopher L. Segura Jr.** *is a Research Structural Engineer at the National Institute of Standards and Technology. He is a member of ACI Committees 133, Disaster Reconnaissance; 318, Structural Concrete Building Code; 369, Seismic Repair and Rehabilitation; and 374, Performance-Based Seismic Design of Concrete Buildings. His research interests include seismic design and assessment of buildings and bridges, laboratory testing, uncertainty quantification, and structural failure investigations.*

ACKNOWLEDGMENTS

The research presented in this paper has been supported in part by the National Institute of Standards and Technology through the ATC 94 project and by the National Science Foundation under award number CMMI-1208192.

REFERENCES

Acevedo, C.; Creagh, A.; Moehle, J. P.; Hassan, W.; and Tanyeri, A. C., 2010, "Seismic Vulnerability of Non-Special Boundary Element of Shear Wall under Axial Force Reversals," Pacific Earthquake Engineering Research Center, Berkeley, CA, 19 pp.

ACI Committee 318, 2011, "Building Code Requirements for Structural Concrete (ACI 318-11) and Commentary (ACI 318R-11)," American Concrete Institute, Farmington Hills, MI, 503 pp.

ACI Committee 318, 2014, "Building Code Requirements for Structural Concrete (ACI 318-14) and Commentary (ACI 318R-14)," American Concrete Institute, Farmington Hills, MI, 520 pp.

Anderson, T. W., and Darling, D. A., 1952, "Asymptotic Theory of Certain 'Goodness of Fit' Criteria Based on Stochastic Processes," *Annals of Mathematical Statistics*, V. 23, No. 2, pp. 193-212. doi: 10.1214/aoms/1177729437

Arteta, C. A., 2015, "Seismic Response Assessment of Thin Boundary Elements of Special Concrete Shear Walls," PhD dissertation, University of California, Berkeley, Berkeley, CA.

Arteta, C. A., and Moehle, J. P., 2023, "Compressive Behavior of Thin Rectangular Boundary Elements," *ACI Structural Journal*, V. 120, No. 2, Mar., pp. 157-170. doi: 10.14359/51737236

Arteta, C. A.; To, D. V.; and Moehle, J. P., 2014, "Experimental Response of Boundary Elements of Code-Compliant Reinforced Concrete Shear Walls," 10th US National Conference on Earthquake Engineering, Earthquake Engineering Research Institute, Anchorage, AK.

ASCE/SEI 41-17, 2017, "Seismic Evaluation and Retrofit of Existing Buildings," American Society of Civil Engineers, Reston, VA.

Bažant, Z. P., 1989, "Identification of Strain-Softening Constitutive Relation from Uniaxial Tests by Series Coupling Model for Localization," *Cement and Concrete Research*, V. 19, No. 6, pp. 973-977. doi: 10.1016/0008-8846(89)90111-7

Birely, A. C.; Lowes, L. N.; and Lehman, D. E., 2015, "Fragility Functions for Flexural Reinforced Concrete Walls," Charles Pankow Foundation, https://www.pankowfoundation.org/site/assets/files/2050/2015_6_24_fragilityfunctions_pankowfinalreport.pdf. (last accessed Jan. 15, 2025)

Coleman, J., and Spacone, E., 2001, "Localization Issues in Force-Based Frame Elements," *Journal of Structural Engineering*, ASCE, V. 127, No. 11, pp. 1257-1265. doi: 10.1061/(ASCE)0733-9445(2001)127:11(1257)

Creagh, A.; Acevedo, C.; Moehle, J. P.; Hassan, W.; and Tanyeri, A. C., 2010, "Seismic Performance of Concrete Special Boundary Element," Pacific Earthquake Engineering Research Center, Berkeley, CA, 18 pp.

Jansen, D. C., and Shah, S. P., 1997, "Effect of Length on Compressive Strain Softening of Concrete," *Journal of Engineering Mechanics*, ASCE, V. 123, No. 1, pp. 25-35. doi: 10.1061/(ASCE)0733-9399(1997)123:1(25)

Kent, D. C., and Park, R., 1971, "Flexural Members with Confined Concrete," *Journal of the Structural Division*, ASCE, V. 97, No. 7, pp. 1969-1990. doi: 10.1061/JSDEAG.0002957

Lowes, L. N.; Lehman, D. E.; Birely, A. C.; Kuchma, D. A.; Marley, K. P.; and Hart, C. R., 2012, "Earthquake Response of Slender Planar Concrete Walls with Modern Detailing," *Engineering Structures*, V. 43, pp. 31-47. doi: 10.1016/j.engstruct.2012.04.040

Mander, J. B.; Priestley, M. J. N.; and Park, R., 1988a, "Observed Stress-Strain Behavior of Confined Concrete," *Journal of Structural Engineering*, ASCE, V. 114, No. 8, pp. 1827-1849. doi: 10.1061/(ASCE)0733-9445(1988)114:8(1827)

Mander, J. B.; Priestley, M. J. N.; and Park, R., 1988b, "Theoretical Stress-Strain Model for Confined Concrete," *Journal of Structural Engineering*, ASCE, V. 114, No. 8, pp. 1804-1826. doi: 10.1061/(ASCE)0733-9445(1988)114:8(1804)

Marafi, N. A.; Ahmed, K. A.; Lehman, D. E.; and Lowes, L. N., 2019, "Variability in Seismic Collapse Probabilities of Solid- and Coupled-Wall Buildings," *Journal of Structural Engineering*, ASCE, V. 145, No. 6, p. 04019047. doi: 10.1061/(ASCE)ST.1943-541X.0002311

Markeset, G., and Hillerborg, A., 1995, "Softening of Concrete in Compression - Localization and Size Effects," *Cement and Concrete Research*, V. 25, No. 4, pp. 702-708. doi: 10.1016/0008-8846(95)00059-L

Massey, F. J., Jr., 1951, "The Kolmogorov-Smirnov Test for Goodness of Fit," *Journal of the American Statistical Association*, V. 46, No. 253, pp. 68-78. doi: 10.1080/01621459.1951.10500769

Massone, L. M.; Polanco, P.; and Herrera, P., 2014, "Experimental and Analytical Response of RC Wall Boundary Elements," 10th US National Conference on Earthquake Engineering, Earthquake Engineering Research Institute, Anchorage, AK.

Moehle, J. P., and Cavanagh, T., 1985, "Confinement Effectiveness of Crossties in RC," *Journal of Structural Engineering*, ASCE, V. 111, No. 10, pp. 2105-2120. doi: 10.1061/(ASCE)0733-9445(1985)111:10(2105)

Monti, G., and Nuti, C., 1992, "Nonlinear Cyclic Behavior of Reinforcing Bars Including Buckling," *Journal of Structural Engineering*, ASCE, V. 118, No. 12, pp. 3268-3284. doi: 10.1061/(ASCE)0733-9445(1992)118:12(3268)

Nakamura, H., and Higai, T., 1999, "Compressive Fracture Energy and Fracture Zone Length of Concrete," US-Japan Seminar on Post-Peak Behavior of Reinforced Concrete Structures Subjected to Seismic Loads: Recent Advances and Challenges on Analysis and Design, Tokyo, Japan.

Razvi, S. R., and Saatcioglu, M., 1999, "Confinement Model for High-Strength Concrete," *Journal of Structural Engineering*, ASCE, V. 125, No. 3, pp. 281-289. doi: 10.1061/(ASCE)0733-9445(1999)125:3(281)

Rustom, A., 2012, *Descriptive Statistics, Probability and Inference: A Conceptual and Applicated Vision*, first edition, Universidad de Chile, Santiago, Chile. (in Spanish)

Saatcioglu, M., and Razvi, S. R., 1992, "Strength and Ductility of Confined Concrete," *Journal of Structural Engineering*, ASCE, V. 118, No. 6, pp. 1590-1607. doi: 10.1061/(ASCE)0733-9445(1992)118:6(1590)

Scott, B. D.; Park, R.; and Priestley, M. J. N., 1982, "Stress-Strain Behavior of Concrete Confined by Overlapping Hoops at Low and High Strain Rates," *ACI Journal Proceedings*, V. 79, No. 1, Jan.-Feb., pp. 13-27. doi: 10.14359/10875

Segura, C. L., and Wallace, J. W., 2018a, "Impact of Geometry and Detailing on Drift Capacity of Slender Walls," *ACI Structural Journal*, V. 115, No. 3, May, pp. 885-895. doi: 10.14359/51702046

Segura, C. L., and Wallace, J. W., 2018b, "Seismic Performance Limitations and Detailing of Slender Reinforced Concrete Walls," *ACI Structural Journal*, V. 115, No. 3, May, pp. 849-859. doi: 10.14359/51701918

Shah, S. P., and Sankar, R., 1987, "Internal Cracking and Strain-Softening Response of Concrete under Uniaxial Compression," *ACI Materials Journal*, V. 84, No. 3, May-June, pp. 200-212. doi: 10.14359/1926

Sheikh, S. A., and Uzumeri, S. M., 1982, "Analytical Model for Concrete Confinement in Tied Columns," *Journal of the Structural Division*, ASCE, V. 108, No. 12, pp. 2703-2722. doi: 10.1061/JSDEAG.0006100

Sritharan, S.; Beyer, K.; Henry, R. S.; Chai, Y. H.; Kowalsky, M.; and Bull, D., 2014, "Understanding Poor Seismic Performance of Concrete Walls and Design Implications," *Earthquake Spectra*, V. 30, No. 1, pp. 307-334. doi: 10.1193/021713EQS036M

Takahashi, S.; Yoshida, K.; Ichinose, T.; Sanada, Y.; Matsumoto, K.; Fukuyama, H.; and Suwada, H., 2013, "Flexural Drift Capacity of Reinforced Concrete Wall with Limited Confinement," *ACI Structural Journal*, V. 110, No. 1, Jan.-Feb., pp. 95-104. doi: 10.14359/51684333

Taleb, R.; Tani, M.; and Kono, S., 2016, "Performance of Confined Boundary Regions of RC Walls under Cyclic Reversal Loadings," *Journal of Advanced Concrete Technology*, V. 14, No. 4, pp. 108-124. doi: 10.3151/jact.14.108

Tripathi, M.; Dhakal, R.; Dashti, F.; and Gokhale, R., 2020, "Axial Response of Rectangular RC Prisms Representing the Boundary Elements of Ductile Concrete Walls," *Bulletin of Earthquake Engineering*, V. 18, No. 9, pp. 4387-4420. doi: 10.1007/s10518-020-00868-2

Wallace, J. W.; Massone, L. M.; Bonelli, P.; Dragovich, J.; Lagos, R.; Luders, C.; and Moehle, J. P., 2012, "Damage and Implications for Seismic Design of RC Structural Wall Buildings," *Earthquake Spectra*, V. 28, pp. 281-299. doi: 10.1193/1.4000047

Wee, T. H.; Chin, M. S.; and Mansur, M. A., 1996, "Stress-Strain Relationship of High-Strength Concrete in Compression," *Journal of Materials in Civil Engineering*, ASCE, V. 8, No. 2, pp. 70-76. doi: 10.1061/(ASCE)0899-1561(1996)8:2(70)

Welt, T. S.; Massone, L. M.; LaFave, J. M.; Lehman, D. E.; McCabe, S. L.; and Polanco, P., 2017, "Confinement Behavior of Rectangular Reinforced Concrete Prisms Simulating Wall Boundary Elements," *Journal of Structural Engineering*, ASCE, V. 143, No. 4, p. 04016204. doi: 10.1061/(ASCE)ST.1943-541X.0001682